Dalton Transactions

ROYAL SOCIETY OF CHEMISTRY

PAPER

View Article Online
View Journal | View Issue

Cite this: *Dalton Trans.*, 2021, **50**, 15359

The influence of the $6s^2$ configuration of Bi^{3+} on the structures of $A'BiNb_2O_7$ (A' = Rb, Na, Li) layered perovskite oxides†

Subhadip Mallick,[a] Guru Khalsa,[b] Jeffrey Z. Kaaret,[c] Weiguo Zhang,[d] Maria Batuk,[e] Alexandra S. Gibbs,[f] Joke Hadermann,[e] P. Shiv Halasyamani,[d] Nicole A. Benedek[b] and Michael A. Hayward *[a]

Received 3rd September 2021,
Accepted 5th October 2021

DOI: 10.1039/d1dt02974f

rsc.li/dalton

Solid state compounds which exhibit non-centrosymmetric crystal structures are of great interest due to the physical properties they can exhibit. The 'hybrid improper' mechanism – in which two non-polar distortion modes couple to, and stabilize, a further polar distortion mode, yielding an acentric crystal structure – offers opportunities to prepare a range of novel non-centrosymmetric solids, but examples of compounds exhibiting acentric crystal structures stabilized by this mechanism are still relatively rare. Here we describe a series of bismuth-containing layered perovskite oxide phases, $RbBiNb_2O_7$, $LiBiNb_2O_7$ and $NaBiNb_2O_7$, which have structural frameworks compatible with hybrid-improper ferroelectricity, but also contain Bi^{3+} cations which are often observed to stabilize acentric crystal structures due to their $6s^2$ electronic configurations. Neutron powder diffraction analysis reveals that $RbBiNb_2O_7$ and $LiBiNb_2O_7$ adopt polar crystal structures (space groups *I2cm* and *B2cm* respectively), compatible with stabilization by a trilinear coupling of non-polar and polar modes. The Bi^{3+} cations present are observed to enhance the magnitude of the polar distortions of these phases, but are not the primary driver for the acentric structure, as evidenced by the observation that replacing the Bi^{3+} cations with Nd^{3+} cations does not change the structural symmetry of the compounds. In contrast the non-centrosymmetric, but non-polar structure of $NaBiNb_2O_7$ (space group $P2_12_12_1$) differs significantly from the centrosymmetric structure of $NaNdNb_2O_7$, which is attributed to a second-order Jahn-Teller distortion associated with the presence of the Bi^{3+} cations.

Introduction

Solid state compounds that crystalize with structures which do not possess inversion symmetry are of great interest because they can exhibit physical properties such as piezoelectricity, ferroelectricity and second harmonic generation (SHG) which are forbidden by symmetry to centrosymmetric materials.[1,2] Unfortunately solids with non-centrosymmetric crystal structures are rare[3] because centrosymmetric packing schemes tend to be thermodynamically preferred to non-centrosymmetric alternatives. A common strategy to counter the general instability of non-centrosymmetric structures utilizes electronically driven structural distortions, such as the second-order Jahn-Teller (SOJT) distortions which drive the off-centring of octahedrally coordinated d^0 transition metal cations (*e.g.* Ti^{4+} in $BaTiO_3$),[4–7] or the distortions driven by the presence of post-transition metal cations with ns^2 electronic configurations (*e.g.* Bi^{3+} in $BiFeO_3$), often thought of as a 'stereoactive lone pair'.[8–13] While this is generally a productive approach for preparing acentric materials, the need to include these specific cations restricts the chemical diversity of non-centrosymmetric materials and makes it hard to include other properties, such as magnetism, in acentric phases.[14]

Recently theory predictions and experimental observations have revealed an alternative mechanism which can be used to stabilize polar crystal structures (a class of non-centrosymmetric structure which is allowed by symmetry to exhibit a spontaneous electrical polarisation). This 'hybrid-improper' mechanism utilizes a combination of two non-polar structural distortions (typically the low energy rotations of the octahedral

[a]*Department of Chemistry, University of Oxford, Inorganic Chemistry Laboratory, South Parks Road, Oxford, OX1 3QR, UK. E-mail: michael.hayward@chem.ox.ac.uk*
[b]*Department of Materials Science and Engineering, Cornell University, Ithaca, NY 14853, USA*
[c]*School of Applied and Engineering Physics, Cornell University, Ithaca, NY 14853, USA*
[d]*Department of Chemistry, University of Houston, 112 Fleming Building, Houston, Texas 77204-5003, USA*
[e]*EMAT, University of Antwerp, Groenenborgerlaan 171, B-2020 Antwerp, Belgium*
[f]*ISIS Facility, Rutherford Appleton Laboratory, Chilton, Oxon OX11 0QX, UK*
†Electronic supplementary information (ESI) available. See DOI: 10.1039/d1dt02974f

units in perovskite phases) to break the inversion symmetry of the host framework and then couple to, and stabilize, a further polar distortion mode.[15–17] As the polar distortions in this class of material are not driven by SOJT-like instabilities, the trilinear-coupled hybrid-improper mechanism offers an opportunity to broaden the chemistry of solids adopting acentric crystal structures.

A symmetry analysis reveals that in the absence of particular cation ordering patterns, the reciprocal nature of the tilting distortions of the 3D perovskite structure prevents the hybrid-improper mechanism from functioning[18] (although it should be noted that tilting distortions are not a *requirement* for the hybrid improper mechanism in general,[19] however these distortions are commonly associated with this mechanism of ferroelectricity in perovskites and related materials). As a consequence most attention has focused on the layered variants of the perovskite structure which can exhibit hybrid-improper polar structures in the absence of cation order.

A complimentary combination of theory and experiment has shown a number of n = 2 Ruddlesden Popper phases including $(Ca, Sr)_3Ti_2O_7$,[20] $Sr_3Zr_2O_7$,[21] $(Ca, Sr)_3Sn_2O_7$ [22] and $Ca_3Mn_2O_7$ [23] are hybrid-improper ferroelectrics. Similarly the n = 2 Dion-Jacobson phases $CsNdM_2O_7$ and $RbNdM_2O_7$ (M = Nb, Ta) have been demonstrated to be ferroelectric and/or polar phases,[24–26] stabilized by trilinear coupling, as have $LiNdNb_2O_7$ and $LiNdTa_2O_7$,[27] pseudo Ruddlesden-Popper phases derived from the corresponding $RbNdM_2O_7$ parent phase *via* Li-for-Rb cation exchange.

It can be seen that many of the reported hybrid improper ferroelectric and polar phases contain octahedrally coordinated d^0 transition metal cations. Thus, in principle, these phase could be susceptible to SOJT-driven polar structural distortions which are potentially in competition with the observed trilinear-coupled hybrid improper polar structures. Indeed, recently we observed that the two polar pseudo Ruddlesden-Popper phases $Li_2La(TaTi)O_7$ and $Na_2La(TaTi)O_7$ exhibit different types of polar distortion.[28] The structure of the Li phase is consistent with a hybrid-improper stabilization mechanism, while the structure of the Na phase is consistent with a conventional SOJT-driven polar distortion indicating that the two mechanisms are in competition in the $La(TaTi)O_7$ perovskite sheets.

Here we describe the preparation and crystallographic analysis of the Dion-Jacobson phase $RbBiNb_2O_7$ and the pseudo Ruddlesden-Popper phases $LiBiNb_2O_7$ and $NaBiNb_2O_7$ derived from it *via* cation exchange, which have been prepared to examine the competition between trilinear-coupled polar distortions and the conventional polar distortions driven by the presence of $6s^2$ Bi^{3+} cations.

Experimental

Synthesis

Polycrystalline samples of $RbBiNb_2O_7$ were prepared by a ceramic synthesis method from Bi_2O_3 (99.995%), Nb_2O_5 (99.9985%, dried at 900 °C) and Rb_2CO_3 (99.8%). Suitable stoichiometric ratios of Bi_2O_3 and Nb_2O_5 were ground together in an agate pestle and mortar and combined with 50% excess of Rb_2CO_3 (to compensate for loss due to volatilization at high temperature). These mixtures were placed in silica crucibles and heated at 600 °C in air for 12 h. The samples were then reground and heated at 1000 °C for 6 h then 12 h and 2 further periods of 4 h with regrinding between heating cycles. Finally, the powder samples were washed with distilled water to remove any excess rubidium oxide and then dried in air at 120 °C for 12 h. This heating regime was required to avoid the formation of $BiNbO_4$.

$LiBiNb_2O_7$ and $NaBiNb_2O_7$ were synthesized by reacting $RbBiNb_2O_7$ with a 10 mole-equivalents of $LiNO_3$ (99.98%) or $NaNO_3$ (>99%) respectively. These mixtures were ground together and loaded into silica crucibles and heated in air for two periods of 48 h at 360 °C. Between heating cycles, the samples were washed with distilled water, dried for 12 h at 120 °C in air and mixed with further 10 mole-equivalents of $LiNO_3$ or $NaNO_3$. After the final heating step, all samples were washed with distilled water to remove the $LiNO_3$ and $NaNO_3$ and then dried for 12 h at 120 °C in air. Samples of $NaBiNb_2O_7$ were dried under flowing oxygen at 350 °C to eliminate all interlayer water and transferred to an argon-filled glovebox for storage.

Characterisation

X-ray powder diffraction data were collected using a PANalytical X'pert diffractometer incorporating an X'celerator position-sensitive detector (monochromatic Cu $K\alpha_1$ radiation). High-resolution synchrotron X-ray powder diffraction (SXRD) data were collected from the I11 instrument at the Diamond Light Source Ltd. Diffraction patterns were collected using Si-calibrated X-rays with an approximate wavelength of 0.825 Å from samples, sealed in 0.3 mm diameter borosilicate glass capillaries. Time of flight neutron powder diffraction (NPD) data were collected using the HRPD diffractometer at the ISIS neutron source from the samples loaded in 8 mm vanadium cans. The sample of $NaBiNb_2O_7$ was sealed under argon prior to measurement to avoid water absorption. Rietveld refinements were performed using TOPAS Academic (V6).[29] The particle-size dependent second harmonic generation (SHG) response of samples was measured by grinding sintered pellets of material and then sieving the resulting powders into distinct particle size ranges (<20, 20–45, 45–63, 63–75, 75–90, 90–125 μm). SHG intensity was then recorded from each particle size range and compared to a standard sample of KH_2PO_4 (KDP) in the same particle size ranges. No index matching fluid was used in any of the experiments. A detailed description of the experimental setup and process has been reported previously.[30]

High angle annular dark field (HAADF) scanning transmission electron microscopy (STEM) images were acquired using a probe aberration corrected FEI Titan 80-300 "cubed" microscope operated at 300 kV. Samples for TEM analysis were prepared in an argon-filled glove box by dipping a copper TEM

grid into the ground dry powder. The grids were then transferred into the microscope using a vacuum transfer holder.

First-principles density functional calculations were performed using the Vienna Ab Initio Simulation Package (VASP).[31–34] The PBEsol exchange-correlation functional[35] and projector-augmented wave potentials[36,37] to represent the ion cores were used for all calculations. The valence electron configurations were as follows: $4s^2 4p^6 5s^1$ for Rb, $1s^2 2s^1$ for Li, $5d^{10} 6s^2 6p^3$ for Bi, $5s^2 5p^6 4f^1 6s^2$ for Nd (three f-electrons in the core), $4s^2 4p^6 4d^4 5s^1$ for Nb and $2s^2 2p^4$ for O. Convergence of the lattice parameters (within 10^{-4} Å) of the high-symmetry parent phase for $RbBiNb_2O_7$ was achieved with a plane wave cutoff of 800 eV and a k-point grid of 8 × 8 × 4 compared to higher plane wave cutoffs and denser grids. A 6 × 6 × 4 k-point grid was used for all calculations on $LiBiNb_2O_7$. A force convergence tolerance of 0.001 Å was used for all calculations. Mode force constants were calculated using density functional perturbation theory.[38]

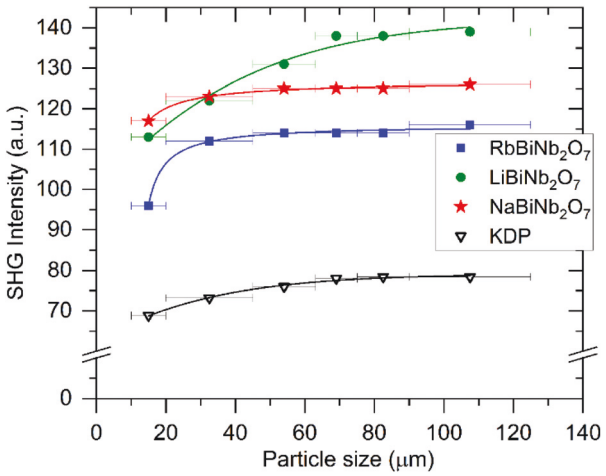

Fig. 1 SHG activity as a function of particle size for A'$BiNb_2O_7$ phases compared to a KDP standard.

Results

Structural characterisation of $RbBiNb_2O_7$

Previously $RbBiNb_2O_7$ has been reported to adopt an n = 2 Dion-Jacobson structure with an $a^-a^-c^+$ tilting distortion, described in space group $P2_1am$.[39] High resolution SXRD and NPD data collected from $RbBiNb_2O_7$ were initially indexed using the reported lattice parameters of $RbBiNb_2O_7$ (a = 5.463 Å, b = 5.393 Å, c = 11.232 Å) which is an $a' \approx \sqrt{2} \times a$, $b' \approx \sqrt{2} \times b$, $c' \approx c$ geometric expansion of the undistorted n = 2 Dion-Jacobson aristotype unit cell. However, close inspection of the diffraction data reveals a series of super lattice peaks which correspond to the doubling of c-lattice parameter (Fig. S1†) indicating the unit cell is in fact an $a' \approx \sqrt{2} \times a$, $b' \approx \sqrt{2} \times b$, $c' \approx 2 \times c$ expansion of the aristotype Dion-Jacobson structure, with extinction conditions consistent with a body-centred unit cell.

Powder SHG measurements indicate $RbBiNb_2O_7$ exhibits SHG activity ~1.8 times that of KDP, as shown in Fig. 1. In addition, $RbBiNb_2O_7$ is reported to exhibit ferroelectric behaviour.[39,40] Both of these observations indicate $RbBiNb_2O_7$ adopts a non-centrosymmetric structure. When combined with the diffraction data, and previous symmetry analysis of the n = 2 Dion-Jacobson framework,[25] these observations are consistent with the $a^-a^-c^+/-(a^-a^-c^+)$ distorted structure previously reported for $RbNdNb_2O_7$.[24] A structural model was constructed for $RbBiNb_2O_7$ based on the $I2cm$ structure of $RbNdNb_2O_7$ and refined against the powder neutron diffraction data collected at room temperature. Both NPD and SXRD data collected from $RbBiNb_2O_7$ exhibit mild (00l) preferred orientation, consistent with the layered structure of the material. This was modelled in the refinement using an 4th order spherical harmonic expression.[41] The refinement proceeded smoothly to give good fit to the data as described in Table 1, with selected bond lengths, angles and bond valence sums[42] in Table 2 and a plot of the fit to the diffraction data in Fig. 2.

Table 1 Parameters from the structural refinement of an $I2cm$ model against the neutron powder diffraction data collected from $RbBiNb_2O_7$ at 298 K

Atom	Site	x	y	z	Occ.	B_{iso} (Å^2)
Rb1	4a	0.7363(9)	0	0	1	1.85(7)
Bi1	4b	0.6981(5)	0.0168(5)	$\frac{1}{4}$	1	1.03(7)
Nb1	8c	0.2473(6)	0.9952(6)	0.3574(1)	1	0.35(5)
O1	8c	0.9897(8)	0.7631(8)	0.3306(2)	1	1.99(10)
O2	8c	0.0616(6)	0.3003(8)	0.3451(2)	1	1.52(9)
O3	8c	0.7479(7)	0.5309(6)	0.4340(1)	1	1.02(7)
O4	4b	0.7813(11)	0.4303(9)	$\frac{1}{4}$	1	1.57(12)

$RbBiNb_2O_7$ – space group $I2cm$ (#46). a = 5.45245(8) Å, b = 5.38185(7) Å, c = 22.4229(3) Å, volume = 657.98(2) Å^3. Formula weight = 592.27 g mol^{-1}, Z = 4. Radiation source: neutron time of flight. Temperature: 298 K. R_p = 6.205%, $_wR_p$ = 7.474%, R_{Bragg} = 3.686%.

Table 2 Selected bond lengths and cation bond valence sums from the refined structure of $RbBiNb_2O_7$

Cation	Anion	Bond length (Å)	BVS
Nb	O1 × 1	1.973(6)	+5.085
	O1 × 1	2.010(6)	
	O2 × 1	2.055(5)	
	O2 × 1	1.949(6)	
	O3 × 1	1.723(4)	
	O4 × 1	2.448(3)	
Bi	O1 × 2	2.613(5)	+2.943
	O1 × 2	2.767(5)	
	O2 × 2	3.287(5)	
	O2 × 2	2.464(5)	
	O4 × 1	2.290(7)	
	O4 × 1	3.189(6)	
	O4 × 1	2.271(6)	
	O4 × 1	3.193(7)	
Rb	O3 × 2	3.051(6)	+0.897
	O3 × 2	2.927(4)	
	O3 × 2	3.218(4)	
	O3 × 2	3.162(6)	

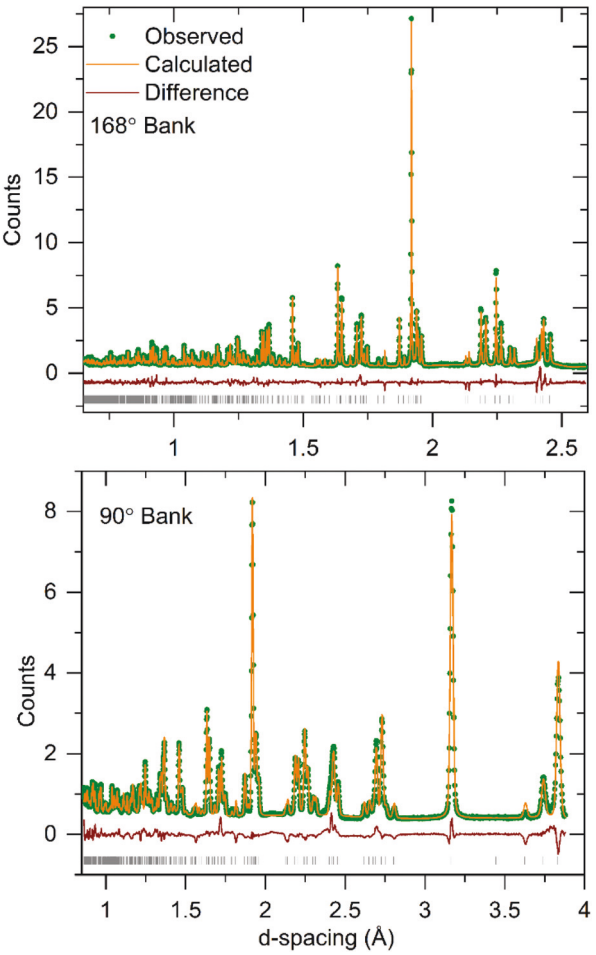

Fig. 2 Observed, calculated and difference plots from the structural refinement of $RbBiNb_2O_7$ against powder neutron diffraction data collected at 298 K.

There is generally excellent agreement between the optimized polar structure of $RbBiNb_2O_7$ obtained from our first-principles calculations and that obtained experimentally, as shown in the ESI.† The lattice parameters and volume of the theoretically optimized structure are within 1% of those measured experimentally. There is also good agreement between theory and experiment regarding the amplitudes of the distortion modes that contribute to the structure of the polar phase, although the amplitudes of the zone-boundary A_5^- and A_2^+ tilt/rotation modes are over-estimated in our first-principles calculations; DFT has a well-known tendency to slightly over-estimate the magnitudes of these kinds of distortions in perovskite and related materials.

Structural characterisation of $LiBiNb_2O_7$

Previous studies describing the Li-for-Rb cation exchange of the Dion-Jacobson phase $RbNdNb_2O_7$ have shown that the resulting material, $LiNdNb_2O_7$, exhibits a Ruddlesden-Popper type structure in which the stacking of the $NdNb_2O_7$ perovskite layers has changed, on cation exchange, to accommodate the small Li^+ cations in pseudo tetrahedral coordination sites, as has been observed in a number of analogous cation exchange reactions.[27,43] SXRD and PND data collected from $LiBiNb_2O_7$ at room temperature can be indexed using an orthorhombic unit cell (a = 5.456 Å, b = 5.341 Å, c = 20.819 Å) consistent with an $a' \approx \sqrt{2} \times a$, $b' \approx \sqrt{2} \times b$, $c' \approx c$ geometric expansion of the undistorted n = 2 Ruddlesden-Popper aristotype unit cell, directly analogous to the reported structure of $LiNdNb_2O_7$. Powder SHG measurements indicate $LiBiNb_2O_7$ exhibits an SHG activity ~2 times that of KDP (Fig. 1) indicating that it adopts a non-centrosymmetric crystal structure. Symmetry analysis of the distortions of the n = 2 Ruddlesden-Popper framework indicates that there are four non-centrosymmetric candidate structures described in space groups $Bb2_1m$, $P2_1nm$, $B2cm$ and $P2cm$ respectively.[27] An analysis of the diffraction data, described in detail in the ESI,† revealed that the best fit to the data was achieved using the model described in space group $B2cm$, confirming that $LiBiNb_2O_7$ adopts an $a^-a^-c^+/-(a^-a^-c^+)$ distorted n = 2 Ruddlesden-Popper structure, analogous to that reported for $LiNdNb_2O_7$.[27] Both NPD and SXRD data collected from $LiBiNb_2O_7$ exhibit (00l) preferred orientation, consistent with the layered structure of the material. This was modelled in the refinement using an 4th order spherical harmonic expression.[41] The refinement proceeded smoothly, with the Li site refining to full occupancy within error. Full details of the refined structure of $LiBiNb_2O_7$ are given in Table 3, with selected bond length, angles and bond valence sums[42] in Table 4 and a plot of the diffraction data in Fig. 3.

Our first-principles calculations of the structure of $LiBiNb_2O_7$ in the polar $B2cm$ phase are also in excellent agreement with that measured experimentally, as shown in the ESI.† In this case, we did not calculate the force constants of the relevant distortion modes and perform further lattice dynamical analysis due to the challenges presented by the Li ordering in the $I4/mmm$ aristotype phase. While it is possible to construct an ordered structure in $Bmcm$ symmetry to approximate the aristotype phase, this is not the same structure that the material 'experiences' in the parent phase and so the relationship between the force constants of the $Bmcm$ phase and the true $I4/mmm$ artisotype structure is unclear.

Table 3 Parameters from the structural refinement of $B2cm$ model against the neutron powder diffraction data collected from $LiBiNb_2O_7$ at 298 K

		x	y	z	Occ.	B_{iso} (Å^2)
Li1	4a	0.9993(52)	0	0	0.99(3)	3.69(4)
Bi1	4c	0.1893(4)	0.7348(6)	$\frac{1}{4}$	1	0.74(9)
Nb1	8d	0.2434(6)	0.7546(6)	0.6347(1)	1	0.30(6)
O1	4c	0.7520(14)	0.6789(7)	$\frac{1}{4}$	1	0.49(10)
O2	8d	0.0501(8)	0.5507(10)	0.3532(2)	1	1.42(10)
O3	8d	0.9878(9)	0.9888(10)	0.8328(2)	1	1.77(11)
O4	4d	0.2361(10)	0.8258(4)	0.5535(2)	1	0.65(7)

$LiBiNb_2O_7$ – space group $B2cm$ (#39). a = 5.4560(2) Å, b = 5.3415(1) Å, c = 20.8186(6) Å, volume = 606.71(3) Å^3. Formula weight = 513.726 g mol^{-1}, Z = 4. Radiation source: neutron time of flight. Temperature: 298 K. R_p = 5.37%, $_wR_p$ = 6.92%, R_{Bragg} = 3.113%.

Table 4 Selected bond lengths and cation bond valence sums from the refined structure of $LiBiNb_2O_7$

Cation	Anion	Bond length (Å)	BVS
Nb	O1 × 1	2.435(3)	+5.032
	O2 × 1	1.958(6)	
	O2 × 1	2.012(6)	
	O3 × 1	1.992(6)	
	O3 × 1	2.028(6)	
	O4 × 1	1.733(5)	
Bi	O2 × 2	2.482(5)	+3.005
	O2 × 2	3.289(5)	
	O3 × 2	2.522(6)	
	O3 × 2	2.732(6)	
	O1 × 1	2.405(8)	
	O1 × 1	2.236(6)	
	O1 × 1	3.150(5)	
	O1 × 1	3.156(11)	
Li	O4 × 2	1.94(2)	+0.973
	O4 × 2	2.04(3)	

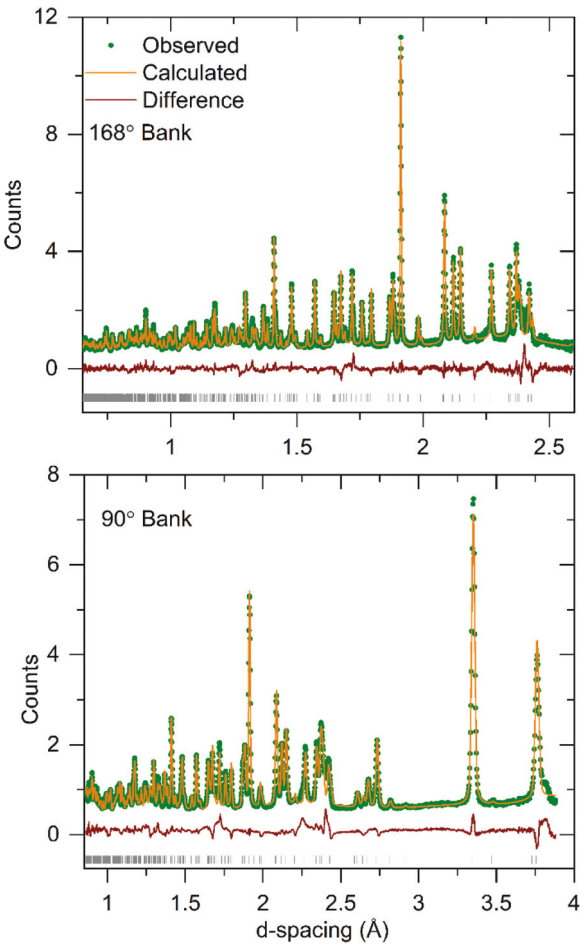

Fig. 3 Observed, calculated and difference plots from the structural refinement of $LiBiNb_2O_7$ against powder neutron diffraction data collected at 298 K.

Structural characterisation of $NaBiNb_2O_7$

High-resolution SXRD and PND data collected from $NaBiNb_2O_7$ can be indexed using an orthorhombic unit cell (a = 5.47 Å, b = 5.38 Å, c = 21.67 Å) which is consistent with an $a' \approx \sqrt{2} \times a$, $b' \approx \sqrt{2} \times b$, $c' \approx c$ geometric expansion of the undistorted aristotype unit cell of n = 2 Ruddlesden-Popper structure. The extinction conditions of the SXRD and NPD data allow us to eliminate the majority of n = 2 Ruddlesden-Popper phases distorted by cooperative tilting on the NbO_6 units[27] leaving 5 candidate structures described in space groups *Pbcm*, *Pnnm*, *Pnam*, $P2_1nm$ and *P2cm*.

Models of these distorted structures were constructed and refined against the NPD data. The model described in space group $P2_1nm$ gave the best fit to the data (Table S3†). However, close inspection of the refined $P2_1nm$ model reveals that the resulting structure is very irregular, with chemically equivalent cations having very different local bonding environments, as evident from the bond valence sums of the metal cations (Table S4, ESI†). To address this problem, constraints were added to the model to make the bond valence sums of chemically equivalent cations the same, resulting in a poor fit to the NPD data as noted in Table S3,† so this model was discarded.

The $a^-a^-c^+/a^-a^-(-c^+)$ distorted model, described in space group *Pnam*, gives the best fit to the data of the remaining models (as shown in Table S3 in the ESI†) and yields a chemically reasonable structure. However, this model is centrosymmetric (incompatible with observed SHG activity, Fig. 1), suggesting that it describes the tilting distortion of the NbO_6 units accurately, but the 'true' structure of $NaBiNb_2O_7$ is subject to a further distortion which breaks the inversion symmetry of this *Pnam* model. Thus we considered the inclusion of Γ point distortion modes in the *Pnam* model with the help of the ISODISTORT software.[44,45] This symmetry analysis yields four candidate non-centrosymmetric models described in space groups $P2_12_12_1$, $Pn2_1m$, $P2_1am$ and $Pna2_1$. Fitting statistics from the refinement of these four non-centrosymmetric models are comparable to one another. However, only the model refined in space group $P2_12_12_1$ yields a chemically plausible structure as described in detail in the ESI.† Both NPD and SXRD data collected from $NaBiNb_2O_7$ exhibit strong (00l) preferred orientation, consistent with the layered structure of the material. This was modelled in the refinement using an 4th order spherical harmonic expression.[41] Full details of the refined structure of $NaBiNb_2O_7$ are given in Table 5, with selected bond lengths, angles and bond valence sums[42] in Table 6 and a plot of the fit to the diffraction data in Fig. 4.

Comparison of the atomic positions in the centrosymmetric *Pnam* model and the acentric $P2_12_12_1$ model reveals that the principal difference between the two structures is the ordering of the Na^+ cations into a chequerboard pattern in the latter model, which is accompanied by a small antiferroelectric displacement of the Bi^{3+} cations, as described in detail in the ESI.†

Microstructural characterisation of $NaBiNb_2O_7$

During structural analysis it was observed that the powder diffraction data collected from $NaBiNb_2O_7$ exhibits strongly

Table 5 Parameters from the structural refinement of a $P2_12_12_1$ model against the neutron powder diffraction data collected from $NaBiNb_2O_7$ at 298 K

Atom	Site	x	y	z	Occ.	B_{iso} (Å^2)
Na	4a	0.991(2)	0.995(3)	0.5047(9)	0.81(4)	0.62(41)
Bi	4a	0.6936(6)	0.2716(7)	0.2510(8)	1	1.80(11)
Nb1	4a	0.7481(12)	0.2610(20)	0.8630(4)	1	0.05*
Nb2	4a	0.2420(11)	0.2330(20)	0.1439(4)	1	0.05*
O1	4a	0.7620(15)	0.6788(9)	0.2495(14)	1	2.31(14)
O2	4a	0.997(2)	0.501(2)	0.8400(6)	1	1.81(14)
O3	4a	0.980(2)	0.014(2)	0.1702(6)	1	1.81(14)
O4	4a	0.454(2)	0.034(2)	0.8488(7)	1	1.12(11)
O5	4a	0.5580(20)	0.4460(20)	0.1571(7)	1	1.12(11)
O6	4a	0.7229(14)	0.279(2)	0.9437(6)	1	0.53(10)
O7	4a	0.2295(14)	0.2046(19)	0.0620(6)	1	0.53(10)

$NaBiNb_2O_7$ – space group $P2_12_12_1$ (#19). a = 5.4711(2) Å, b = 5.3841(2) Å, c = 21.6750(8) Å, volume = 638.48(4) Å^3. Formula weight = 529.78 g mol^{-1}, Z = 4. Radiation source: neutron time of flight. Temperature: 298 K. R_p = 6.13%, $_wR_p$ = 6.35%, R_{Bragg} = 2.854%. * values not refined.

Table 6 Selected bond lengths from the refined structure of $NaBiNb_2O_7$

Cation	Anion	Bond length (Å)	BVS
Nb1	O1 × 1	2.48(4)	+4.8630
	O2 × 1	1.942(15)	
	O3 × 1	1.983(17)	
	O4 × 1	2.044(14)	
	O5 × 1	2.047(15)	
	O6 × 1	1.757(16)	
Nb2	O1 × 1	2.36(4)	+5.092
	O2 × 1	1.929(14)	
	O3 × 1	1.942(16)	
	O4 × 1	1.950(15)	
	O5 × 1	2.094(14)	
	O7 × 1	1.783(16)	
Bi	O1 × 1	3.121(9)	+2.960
	O1 × 1	2.224(7)	
	O1 × 1	3.214(7)	
	O1 × 1	2.376(9)	
	O2 × 1	2.957(17)	
	O2 × 1	2.665(18)	
	O3 × 1	2.729(19)	
	O3 × 1	2.578(19)	
	O4 × 1	3.224(18)	
	O4 × 1	2.50(3)	
	O5 × 1	3.202(17)	
	O5 × 1	2.36(3)	
Na	O6 × 1	2.383(19)	+0.989
	O6 × 1	2.244(19)	
	O7 × 1	2.37(2)	
	O7 × 1	2.30(2)	

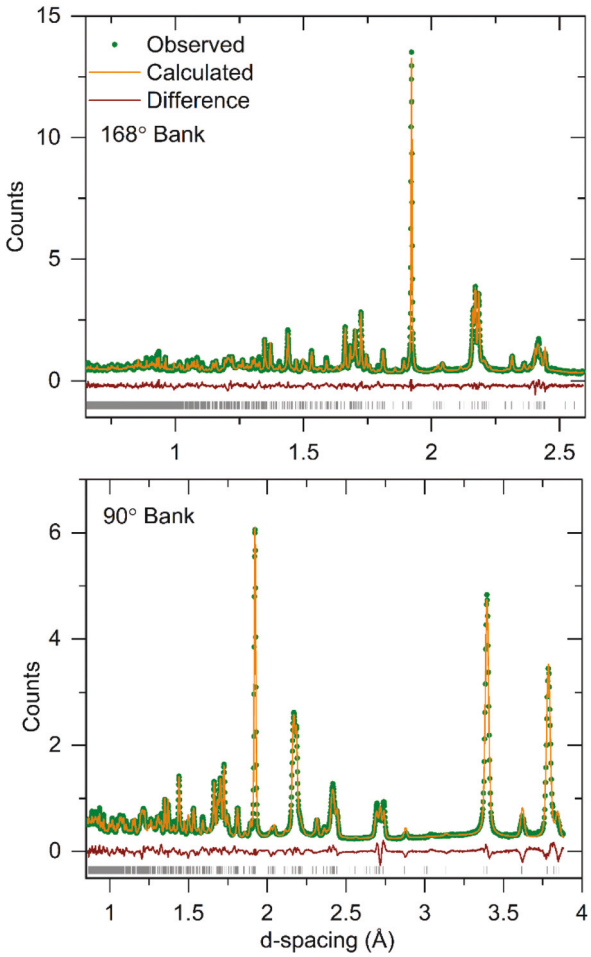

Fig. 4 Observed, calculated and difference plots from the structural refinement of $NaBiNb_2O_7$ against powder neutron diffraction data collected at 298 K.

hkl-dependent peak widths. Fig. 5 shows a small section ($16 < 2\theta/° < 24$) of the SXRD data collected from $LiBiNb_2O_7$ and $NaBiNbO_7$, with the central panel plotting the full-width at half-maximum (FWHM) of each of the observed peaks as a function of 2θ. The widths of the peaks in the $LiBiNb_2O_7$ diffraction pattern is relatively uniform ranging from 0.0508° to 0.0705° across this angular range. In contrast the widths of the peaks in the $NaBiNb_2O_7$ data range from 0.0617° to 0.1331°, with three peaks ([115], [117] and [0010]) being significantly broader than the others. During the structural refinement of $NaBiNb_2O_7$ this variation in peak width, which is also observed in the NPD data, was modelled using an anisotropic lineshape broadening function described by Stephens[46] implemented in the structural model, as described in detail in the ESI.† However, we were interested in determining the origin of this broadening phenomena so undertook a microstructural study of the material. HAADF-STEM images collected from the $NaBiNb_2O_7$ sample revealed extensive intergrowths of other phases derived from $RbBiNb_2O_7$. Fig. 6 shows a HAADF-STEM image in which layers of $NaBiNb_2O_7$ are intergrown with an Aurivillius type phase (thought to be $Na_{0.5}Bi_{2.5}Nb_2O_9$)[47] and a perovskite phase, thought to be $NaNbO_3$. Other images show Dion-Jacobson type stacking (presumably unreacted $RbBiNb_2O_7$) intergrown with layers of $BiNbO_4$ (Fig. S8, ESI†).

Annealing samples of $NaBiNb_2O_7$ in air at 600 °C leads to decomposition to form $NaNbO_3$, and the Aurivillius phases $Na_{0.5}Bi_{2.5}Nb_2O_9$, $Na_{2.5}Bi_{2.5}Nb_4O_{15}$, $Na_{3.5}Bi_{2.5}Nb_5O_{18}$.

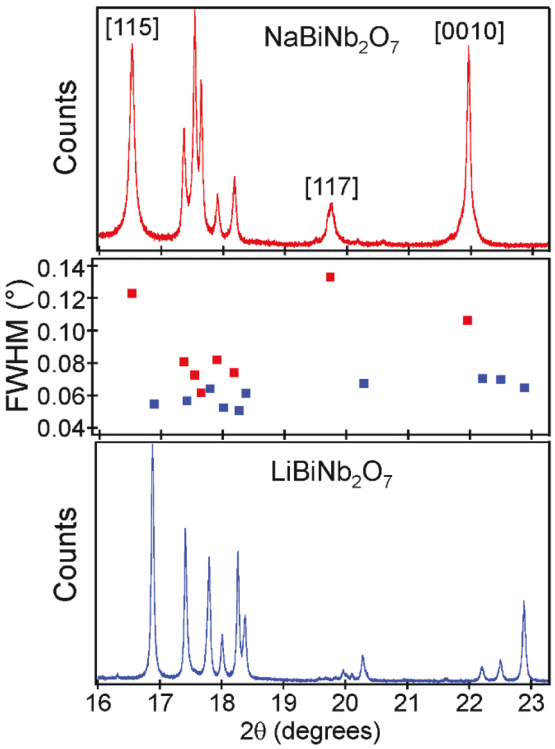

Fig. 5 SXRD data collected from $NaBiNb_2O_7$ (top) and $LiBiNb_2O_7$ (bottom) in the range $16 < 2\theta/° < 20$. Central panel plots the FWHM of the diffraction peaks of $NaBiNb_2O_7$ (red) and $LiBiNb_2O_7$ (blue) as a function of 2θ.

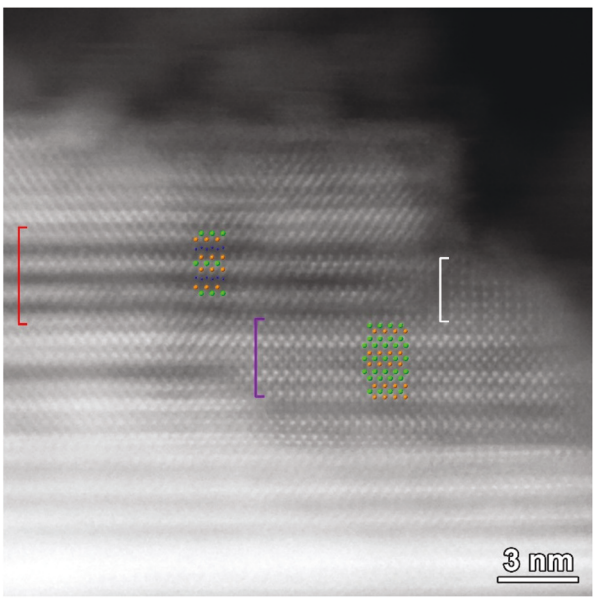

Fig. 6 HAADF-STEM image of the layered crystal. Red bracket: [100] of target phase $NaBiNb_2O_7$. Violet bracket: [110] of Aurivillius type structure $Bi_{2.5}Na_{0.5}Nb_2O_9$: ($A2_1am$, a = 5.49 Å, b = 5.46 Å, c = 24.92 Å). White: perovskite-type blocks. The models are inserted: green – Bi, orange – Nb, blue – Na.

Discussion

$RbBiNb_2O_7$ adopts a polar, n = 2 Dion-Jacobson structure with an $a^-a^-c^+/-(a^-a^-c^+)$ tilting distortion, analogous to that of $RbNdNb_2O_7$.[24] This is in contrast, to the n = 2 Dion-Jacobson phases $CsBiNb_2O_7$ and $CsNdNb_2O_7$ which adopt $a^-a^-c^+/a^-a^-c^+$ tilting distortions.[48] The differing structural distortions adopted by the two $A'NdNb_2O_7$ phases have been rationalized on the basis of a competition between optimizing the bonding of the A′-cation and minimizing the oxygen–oxygen anion repulsion, with the $a^-a^-c^+/a^-a^-c^+$ and $a^-a^-c^+/-(a^-a^-c^+)$ tilting distortions achieving the best compromise for Cs and Rb respectively.[24] The same explanation can be used to rationalize the differing structures of $RbBiNb_2O_7$ and $CsBiNb_2O_7$, in line with calculations which predict that all $RbANb_2O_7$ n = 2 Dion Jacobson phases should adopt a $a^-a^-c^+/-(a^-a^-c^+)$ tilting distortion in their ground states.[24]

Reaction of $RbBiNb_2O_7$ with $LiNO_3$ or $NaNO_3$ yields the pseudo Ruddlesden-Popper phases $LiBiNb_2O_7$ or $NaBiNb_2O_7$ respectively, in which the Li^+ and Na^+ cations reside in tetrahedral coordination sites between the $BiNb_2O_7$ perovskite sheets as shown in Fig. 7. There are two tetrahedral coordination sites per formula unit in the pseudo Ruddlesden-Popper structure. The Li^+ and Na^+ cations occupy half of these sites in ordered arrangements. The Li^+ cations in $LiBiNb_2O_7$ adopt a striped arrangement analogous to that adopted by the Li^+ cations in $LiNdNb_2O_7$. In contrast, the Na^+ cations in $NaBiNb_2O_7$ adopt a chequerboard pattern, analogous to the Na^+ cations in $NaNdNb_2O_7$. The differing cation ordering patterns adopted by the Li^+ and Na^+ cations in the $A'NdNb_2O_7$ phases have been attributed to a competition between minimizing the repulsion between the A′-cations and optimization of the bonding of the Nd^{3+} A-cations, with stripe and chequerboard order being the optimum solution of the Li^+ and Na^+ cations respectively.[27] Again, similar arguments can be made for the analogous Bi-containing phases.

The Li-for-Rb cation exchange of $RbBiNb_2O_7$ with $LiNO_3$ appears to proceed in a purely topochemical manner to yield $LiBiNb_2O_7$ in a direct analogy to the reaction between $RbNdNb_2O_7$ and $LiNO_3$.[27] In contrast, the Na-for-Rb cation exchange reaction between $RbBiNb_2O_7$ and $NaNO_3$ is accompanied by some non-topochemical processes which result in the formation of some $NaNbO_3$ and $Na_{0.5}Bi_{2.5}Nb_2O_9$ (the thermodynamically most stable combination for the $NaBiNb_2O_7$ composition) intergrown into the main $NaBiNb_2O_7$ phase. This partial decomposition of the $A'BiNb_2O_7$ framework on Na exchange, which is not observed in the analogous reaction between $RbNdNb_2O_7$ and $NaNO_3$,[27] suggests that the replacement of Nd^{3+} by Bi^{3+} lowers the activation barriers for non-topochemical processes in the $RbANb_2O_7$ system.

The preparation of the three $A'BiNb_2O_7$ (A′ = Rb, Li, Na) phases which have the same basic structural framework as the corresponding $A'NdNb_2O_7$ phases provides an opportunity to examine the influence of the $6s^2$ electronic configuration of Bi^{3+} on the structural distortions of these layered perovskite materials. The cooperative tilting distortions of perovskite

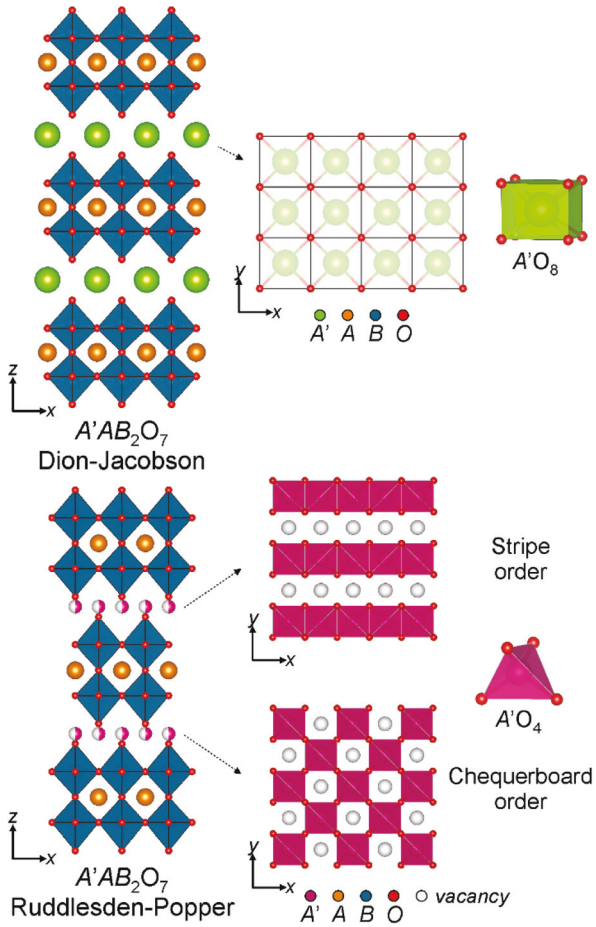

Fig. 7 Structures of the aristotype $A'AB_2O_7$ Dion-Jacobson and Ruddlesden-Popper phases. The A′ cations can adopt striped of chequerboard ordering schemes within the interlayer tetrahedral coordination sites.

phases and layered analogues are typically driven by a mismatch between the size of the A′/A-cations and the B-cations, which is conveniently parameterized by the Goldschmidt tolerance factor $t = \langle A\text{–}O\rangle/(\sqrt{2} \times \langle B\text{–}O\rangle)$.[49] The tolerance factor of a compound can be calculated from tabulated values of the ionic radii, or by extracting the average A–O and B–O bond lengths from an experimental crystal structure. Table 7 shows that values calculated for $RbBiNb_2O_7$ and $RbNdNb_2O_7$ by both methods are similar, with the value for $RbNdNb_2O_7$ being smaller than the Bi analogue by either method, leading to the expectation that $RbNdNb_2O_7$ will have a more distorted structure than $RbBiNb_2O_7$, if Bi^{3+} acts as a purely 'spherical' cation.

We can analyse the structures of the $RbANb_2O_7$ phases in terms of the distortion modes which need to be applied to the aristotype Dion-Jacobson structure (Fig. 7) to achieve the observed distorted structure.[44,45] In the case of $RbBiNb_2O_7$ and $RbNdNb_2O_7$ the *I2cm* symmetry is established by applying a symmetry mode which transforms as the A_5^- irreducible representation of the *P4/mmm* aristotype symmetry, which principally describes the $a^-a^-c^0/-(a^-a^-c^0)$ tilting distortion; a mode which transforms as A_2^+, which principally describes the $a^0a^0c^+/-(a^0a^0c^+)$ tilting distortion and a polar mode which transforms as Γ_5^-, as shown in Fig. 8. The atom displacements which occur on lowering the symmetry from the *P4/mmm* aristotype phase to the observed *I2cm* symmetry structure can then be deconvoluted into contributions from the 3 distortion modes allowing the amplitude of each of the distortion modes to be evaluated,[44,45] as described in detail in the ESI.†

Table 7 shows that the A_5^- distortion of $RbNdNb_2O_7$ is larger than that of $RbBiNb_2O_7$, both when measured in terms of the distortion mode amplitude and the magnitude of the NbO_6 tilting, in line with tolerance factor predictions. The size of the A_2^+ distortion is essentially equal for the two phases, although it is interesting to note that the A_2^+ distortion mode of $RbBiNb_2O_7$ is associated with a much larger instability (more negative force constant, Table 7) than that of $RbNdNb_2O_7$, even though this mode does not involve displacement of the Bi/Nd cations. The Γ_5^- polar distortion, however, is more than 30% larger for $RbBiNb_2O_7$ compared to $RbNdNb_2O_7$ and the Γ_5^- instability is also larger in $RbBiNb_2O_7$ (−3.101 eV Å^{-2}) compared to $RbNdNb_2O_7$ (−2.347 eV Å^{-2}), as shown in Table 7. At first sight this is surprising as the Γ_5^- mode arises from a coupling of the A_5^- and A_2^+ modes *via* the

Table 7 Tolerance factors and distortion mode amplitudes extracted from the refined structures of $A'ANb_2O_7$ phases. Force constants for the distortion modes of the aristotype (*P4/mmm*) structures of $RbNdNb_2O_7$ (from ref. 23) and $RbBiNb_2O_7$. Negative values indicate an energy lowering distortion

	Tolerance factor		A_5^- $a^-a^-c^0/-(a^-a^-c^0)$			A_2^+ $a^0a^0c^+/-(a^0a^0c^+)$			Polar Γ_5^-	
	Ionic radii	Bond lengths	a^- tilt angle (°)	Mode magnitude	Force constant (eV Å^{-2})	c^+ tilt angle (°)	Mode magnitude	Force constant (eV Å^{-2})	Mode magnitude	Force constant (eV Å^{-2})
$RbNdNb_2O_7$	0.925	0.958	7.49	0.785	−2.347	7.57	0.510	−0.486	0.432	−0.866
$RbBiNb_2O_7$	0.964	0.965	5.85	0.560	−3.101	7.70	0.518	−2.080	0.582	−2.984

	Tolerance factor		X_4^- $a^-a^-c^0/-(a^-a^-c^0)$		X_2^+ $a^0a^0c^+/-(a^0a^0c^+)$		Polar Γ_5^-
	Ionic radii	Bond lengths	a^- tilt angle (°)	Mode magnitude	c^+ tilt angle (°)	Mode magnitude	Mode magnitude
$LiNdNb_2O_7$	0.925	0.956	9.62	0.957	6.98	0.565	0.629
$LiBiNb_2O_7$	0.964	0.957	8.06	0.819	7.10	0.474	0.456

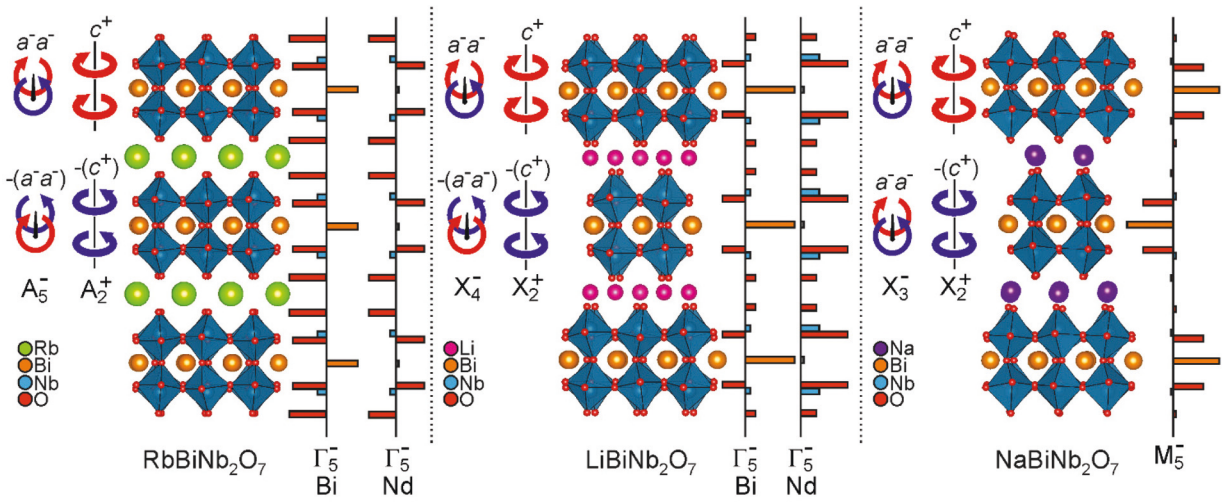

Fig. 8 The structural distortions of $A'ANb_2O_7$ (A' = Rb, Li, Na; A = Nd, Bi) phases. The distortion modes relate the experimental structures to the *P*4/*mmm* or *I*4/*mmm* aristotype structures. The lengths of the solid bars represent the magnitudes and relative directions of the displacements due to the Γ-point polar distortions of $RbBiNb_2O_7$, $RbNdNb_2O_7$, $LiBiNb_2O_7$ and $LiNdNb_2O_7$, and the M_5^- anti-polar distortion of $NaBiNb_2O_7$.

trilinear-coupled hybrid improper mechanism,[15,50] so the larger combined amplitude of the A_5^- and A_2^+ modes for $RbNdNb_2O_7$ might be expected to yield a larger polar distortion for this phase. However, close inspection of the atom displacements associated with the Γ_5^- distortion reveals that the Bi^{3+} cation contributes more than 25% of the total Γ_5^- mode displacement in $RbBiNb_2O_7$, compared to less than 4% from Nd^{3+} in $RbNdNb_2O_7$, as shown in Fig. 8. This suggests that while the trilinear coupling of the A_5^- and A_2^+ modes may establish the *I*2*cm* symmetry of the phase and thus a non-zero amplitude for the Γ_5^- mode, the $6s^2$ electronic configuration of Bi^{3+} enhances the Bi polar displacement *via* an SOJT/stereoactive lone pair, resulting in a larger polar distortion and greater degree of SHG activity for $RbBiNb_2O_7$ compared to $RbNdNb_2O_7$. A similar result was found for $CsBiNb_2O_7$ in previous work;[50] despite the presence of a very large Γ_5^- instability in the aristotype *P*4/*mmm* phase, the largest energy lowering was achieved in the polar $P2_1am$ structure in which the Γ_5^- mode couples with the nonpolar M_2^+ and M_5^- modes. The largest contribution to the polarization in the polar phase came from the Bi–O layers. This is in contrast to the other Dion-Jacobson phases considered in ref. 50 that did not contain Bi – in those materials, the largest contribution to the polarization came from the Nb–O layers.

A similar analysis can be performed on the distorted structures of $LiBiNb_2O_7$ and $LiNdNb_2O_7$,[27] which reveals that three significant distortions are required to establish the *B*2*cm* symmetry of these phases: a symmetry mode which transforms as the X_4^- irreducible representation of the *I*4/*mmm* aristotype symmetry, which principally describes the $a^-a^-c^0/-(a^-a^-c^0)$ tilting distortion; a mode which transforms as X_2^+, which principally describes the $a^0a^0c^+/-(a^0a^0c^+)$ tilting distortion and a polar mode which transforms as Γ_5^-, as shown in Fig. 8.

As shown in Table 7, the X_4^- distortion of $LiNdNb_2O_7$ is larger than that of the Bi analogue, both in terms of the distortion mode amplitude and the degree of NbO_6 tilting. The magnitude of the $a^0a^0c^+/-(a^0a^0c^+)$ tilting associated with the X_2^+ distortion mode is very similar for the two Li phases, but a large Li^+ displacement observed in $LiNdNb_2O_7$ but not $LiBiNb_2O_7$ means the X_2^+ mode amplitude is significantly larger for the Nd^{3+} phase. The Γ_5^- mode amplitude of $LiNdNb_2O_7$ is nearly 40% larger than that of $LiBiNb_2O_7$, consistent with the larger X_3^- and X_2^+ distortions of the Nd phase. However close inspection reveals that the Bi^{3+} cation accounts for 45% of the Γ_5^- displacement, compared to less than 4% from Nd^{3+} in $LiNdNb_2O_7$ (Fig. 8, Tables S9 and S10†), again suggesting the $6s^2$ electronic configuration of Bi^{3+} enhances the polar displacement of the Bi cation.

Despite the partial decomposition of the material on cation exchange, it is still possible to structurally characterise $NaBiNb_2O_7$ and determine that it adopts an $a^-a^-c^+/a^-a^-(-c^+)$ tilting distortion described in space group $P2_12_12_1$, which is non-centrosymmetric, but non-polar. This distortion differs significantly to the centrosymmetric $a^-b^0c^0/b^0a^-c^0$ distortion adopted by $NaNdNb_2O_7$, described in space group $P4_2/mnm$.[27] It is therefore clear that replacement of Nd^{3+} with Bi^{3+} in $NaANb_2O_7$ leads to a much more distorted structure, despite the smaller tolerance factor for the Nd phase. However, it is instructive to look more closely at the details of this structural change.

Close examination of the structures of $RbANb_2O_7$ and $LiANb_2O_7$ reveals that the A-cations in both structural frameworks reside on 12-coordinate sites with ..*m* point symmetry (site 4b for *I*2*cm* symmetry $RbANb_2O_7$; site 4c in *B*2*cm* symmetry $LiANb_2O_7$). These low symmetry coordination sites appear to be compatible with the expected asymmetric coordination geometry of a $6s^2$ Bi^{3+} cation, thus there is no change in structure on replacement of Nd with Bi in either the $RbANb_2O_7$ or $LiANb_2O_7$ system and we can conclude that while the presence of Bi^{3+} enhances the polar distortions of these

phases, it is not the primary driver for the polar structures adopted.

In contrast, the Nd^{3+} cations in $NaNdNb_2O_7$ reside on a 4f site with *m*.2*m* point symmetry. This high symmetry (*x*, *x*, 0) crystallographic site appears to be incompatible with the expected asymmetric coordination of Bi^{3+}. On substitution of Nd^{3+} with Bi^{3+} the tilting distortion of the framework changes to an $a^-a^-c^+/a^-a^-(-c^+)$ arrangement, despite the tolerance factor being slightly larger for $NaBiNb_2O_7$ compared to $NaNdNb_2O_7$. This change in the tilting has the effect of lowering the Bi^{3+} cation site symmetry to ..*m* in the *Pnam* model without cation ordering (4c site) which becomes a 4a, general position in the Na site-ordered $P2_12_12_1$ structure. A distortion mode analysis of the $P2_12_12_1$ structure of $NaBiNb_2O_7$ reveals that while there are 7 modes which are allowed on descending in symmetry from the *I*4/*mmm* aristotype structure, as described in the ESI,† only three have significant amplitudes: a mode which transforms as the X_3^- irreducible representation of the *I*4/*mmm* aristotype symmetry, which principally describes the $a^-a^-c^0/a^-a^-c^0$ tilting distortion; a mode which transforms as X_2^+, which principally describes the $a^0a^0c^+/a^0a^0(-c^+)$ tilting distortion and a mode which transforms as M_5^- which principally describes the antiferroelectric displacement of the Bi^{3+} cations parallel to the *x*-axis, as shown in Fig. 8. Examining the atom displacements associated with these modes, it can be seen that the Bi^{3+} contributes ~52% of the amplitude of the M_5^- mode, consistent with the off-centering of the $6s^2$ Bi^{3+} cations having a significant role in the more distorted structure adopted by $NaBiNb_2O_7$ compared to $NaNdBi_2O_7$.

While, as noted above, the presence of Bi^{3+} is not the primary driver for the structural distortions adopted by $RbBiNb_2O_7$ and $LiBiNb_2O_7$, structural changes on Bi-for-Nd cation substitution have been observed in non-centrosymmetric $n = 3$ Dion-Jacobson phases.[51,52] For example, a computational analysis of the structural distortions of $CsBi_2Ti_2NbO_{10}$ reveals that this phase is a 'proper' ferroelectric in which the principal energy gain on lowering the symmetry of the aristotype structure to the observed *Ima*2 symmetry arises from the Γ-point ferroelectric distortion mode, attributable to an SOJT-like distortion of the Bi^{3+} cations. In contrast, the acentric structure observed for $CsNd_2Ti_2NbO_{10}$ appears to be 'improper' and driven by a trilinear coupling of non-polar distortion modes.

Conclusions

The structures adopted by $A'BiNb_2O_7$ phases compared to the corresponding $A'NdNb_2O_7$ compounds show that the incorporation of 'non-spherical' Bi^{3+} cations can strongly perturb the structures of layered perovskite oxides. In the $NaANb_2O_7$ system, the presence of Bi^{3+} leads to an $a^-a^-c^+/a^-a^-(-c^+)$ tilting distortion and a non-centrosymmetric structure, compared to the $a^-b^0c^0/b^0a^-c^0$ distortion adopted by $NaNdNb_2O_7$ despite the latter phase having the smaller tolerance factor.

In the case of the polar $RbANb_2O_7$ and $LiANb_2O_7$ phases the analogous Nd and Bi materials are isostructural. However the magnitude of the polar distortion mode is enhanced in both Bi materials, again attributable to the non-spherical nature of the $6s^2$ Bi^{3+} cation.

Author contributions

SM prepared the samples and performed the structural analysis, GK and JZK performed the DFT calculations, WZ and PSH collected the SHG data, MB and JH collected the microscopy data, ASG assisted with the collection of the NPD data, NAB supervised the DFT calculations and jointly conceived the study, MAH jointly conceived the study, wrote the manuscript and supervised the study.

Conflicts of interest

There are no conflicts to declare.

Acknowledgements

Experiments at the Diamond Light Source were performed as part of the Block Allocation Group award "Oxford/Warwick Solid State Chemistry BAG to probe composition-structure-property relationships in solids" (EE18786). Experiments at the ISIS pulsed neutron facility were supported by a beam time allocation from the STFC (RB 2000148). SM thanks Somerville College for an Oxford Ryniker Lloyd scholarship. PSH and WZ thank the National Science Foundation (DMR-2002319) and Welch Foundation (E-1457) for support. GK and NB thank the National Science Foundation (DMR-1719875) for support, JZK thanks the Department of Energy Office of Basic Energy Sciences (DE-SC0019414) for support.

Notes and references

1 M. E. Lines and A. M. Glass, *Principles and Applications of Ferroelectrics and Related Materials*, Oxford University Press, Oxford, 1991.
2 F. J. Nye, *Physical Properties of Crystals*, Oxford University Press, Oxford, UK, 1957.
3 P. Halasyamani and K. R. Poeppelmeier, *Chem. Mater.*, 1998, **10**, 2753–2769.
4 R. E. Cohen, *Nature*, 1992, **358**, 136–138.
5 S. K. Kang, H. Tang and T. A. Albright, *J. Am. Chem. Soc.*, 1993, **115**, 1971–1981.
6 M. Kunz and I. D. Brown, *J. Solid State Chem.*, 1995, **115**, 395–406.
7 R. G. Pearson, *J. Mol. Struct.: THEOCHEM*, 1983, **12**, 25–34.
8 I. Lefebvre, M. Lannoo, G. Allan, A. Ibanez, J. Fourcade, J. C. Jumas and E. Beaurepaire, *Phys. Rev. Lett.*, 1987, **59**, 2471–2474.

9 I. Lefebvre, M. A. Szymanski, J. Olivier-Fourcade and J. C. Jumas, *Phys. Rev. B: Condens. Matter Mater. Phys.*, 1998, **58**, 1896–1906.
10 R. Seshadri and N. A. Hill, *Chem. Mater.*, 2001, **13**, 2892–2899.
11 M. W. Stoltzfus, P. M. Woodward, R. Seshadri, J. H. Klepeis and B. Bursten, *Inorg. Chem.*, 2007, **46**, 3839–3850.
12 G. W. Watson and S. C. Parker, *J. Phys. Chem. B*, 1999, **103**, 1258–1262.
13 G. W. Watson, S. C. Parker and G. Kresse, *Phys. Rev. B: Condens. Matter Mater. Phys.*, 1999, **59**, 8481–8486.
14 N. A. Hill, *J. Phys. Chem. B*, 2000, **104**, 6694–6709.
15 N. A. Benedek and C. J. Fennie, *Phys. Rev. Lett.*, 2011, **106**, 107204.
16 A. T. Mulder, N. A. Benedek, J. M. Rondinelli and C. J. Fennie, *Adv. Funct. Mater.*, 2013, **23**, 4810–4820.
17 N. A. Benedek, A. T. Mulder and C. J. Fennie, *J. Solid State Chem.*, 2012, **195**, 11–20.
18 J. M. Rondinelli and C. J. Fennie, *Adv. Mater.*, 2012, **24**, 1961–1968.
19 F. Delodovici, P. Barone and S. Picozzi, *Phys. Rev. Mater.*, 2021, **5**, 064405.
20 Y. S. Oh, X. Luo, F. T. Huang, Y. Z. Wang and S. W. Cheong, *Nat. Mater.*, 2015, **14**, 407–413.
21 S. Yoshida, K. Fujita, H. Akamatsu, O. Hernandez, A. Sen Gupta, F. G. Brown, H. Padmanabhan, A. S. Gibbs, T. Kuge, R. Tsuji, S. Murai, J. M. Rondinelli, V. Gopalan and K. Tanaka, *Adv. Funct. Mater.*, 2018, **28**, 1801856.
22 S. Yoshida, H. Akamatsu, R. Tsuji, O. Hernandez, H. Padmanabhan, A. Sen Gupta, A. S. Gibbs, K. Mibu, S. Murai, J. M. Rondinelli, V. Gopalan, K. Tanaka and K. Fujita, *J. Am. Chem. Soc.*, 2018, **140**, 15690–15700.
23 M. F. Liu, Y. Zhang, L. F. Lin, L. Lin, S. W. Yang, X. Li, Y. Wang, S. Z. Li, Z. B. Yan, X. Z. Wang, X. G. Li, S. Dong and J. M. Liu, *Appl. Phys. Lett.*, 2018, **113**, 022902.
24 T. Zhu, T. Cohen, A. S. Gibbs, W. Zhang, P. S. Halasyamani, M. A. Hayward and N. A. Benedek, *Chem. Mater.*, 2017, **29**, 9489–9497.
25 T. Zhu, A. S. Gibbs, N. A. Benedek and M. A. Hayward, *Chem. Mater.*, 2020, **32**, 4340–4346.
26 S. Asaki, H. Akamatsu, G. Hasegawa, T. Abe, Y. Nakahira, S. Yoshida, C. Moriyoshi and K. Hayashi, *Jpn. J. Appl. Phys.*, 2020, **59**, 6.
27 T. Zhu, G. Khalsa, D. M. Havas, A. S. Gibbs, W. Zhang, P. Halasyamani, N. A. Benedek and M. A. Hayward, *Chem. Mater.*, 2018, **30**, 8915–8924.
28 S. Mallick, A. D. Fortes, W. Zhang, P. S. Halasyamani and M. A. Hayward, *Chem. Mater.*, 2021, **33**, 2666–2672.
29 A. A. Coelho, *Bruker AXS*, Karlsruhe, Germany, 2016.
30 K. M. Ok, E. O. Chi and P. S. Halasyamani, *Chem. Soc. Rev.*, 2006, **35**, 710–717.
31 G. Kresse and J. Hafner, *Phys. Rev. B: Condens. Matter Mater. Phys.*, 1993, **47**, 558–561.
32 G. Kresse and J. Hafner, *Phys. Rev. B: Condens. Matter Mater. Phys.*, 1994, **49**, 14251–14269.
33 G. Kresse and J. Furthmuller, *Comput. Mater. Sci.*, 1996, **6**, 15–50.
34 G. Kresse and J. Furthmuller, *Phys. Rev. B: Condens. Matter Mater. Phys.*, 1996, **54**, 11169–11186.
35 J. P. Perdew, A. Ruzsinszky, G. I. Csonka, O. A. Vydrov, G. E. Scuseria, L. A. Constantin, X. L. Zhou and K. Burke, *Phys. Rev. Lett.*, 2008, **100**, 136406.
36 P. E. Blochl, *Phys. Rev. B: Condens. Matter Mater. Phys.*, 1994, **50**, 17953–17979.
37 G. Kresse and D. Joubert, *Phys. Rev. B: Condens. Matter Mater. Phys.*, 1999, **59**, 1758–1775.
38 S. Baroni, S. de Gironcoli, A. Dal Corso and P. Giannozzi, *Rev. Mod. Phys.*, 2001, **73**, 515–562.
39 B. W. Li, M. Osada, T. C. Ozawa and T. Sasaki, *Chem. Mater.*, 2012, **24**, 3111–3113.
40 C. Chen, H. P. Ning, S. Lepadatu, M. Cain, H. X. Yan and M. J. Reece, *J. Mater. Chem. C*, 2015, **3**, 19–22.
41 M. Jarvinen, *J. Appl. Crystallogr.*, 1993, **26**, 525–531.
42 N. E. Brese and M. O'Keeffee, *Acta Crystallogr., Sect. B: Struct. Sci.*, 1991, **47**, 192–197.
43 M. A. Hayward, in *Comprehensive Inorganic Chemistry II*, ed. J. Reedijk and K. R. Poeppelmeier, Elsevier, Oxford, 2013, vol. 2, pp. 417–453.
44 B. J. Campbell, H. T. Stokes, D. E. Tanner and D. M. Hatch, *J. Appl. Crystallogr.*, 2006, **39**, 607–614.
45 H. T. Stokes, D. M. Hatch and B. J. Campbell, *iso.byu.edu*, 2007.
46 P. W. Stephens, *J. Appl. Crystallogr.*, 1999, **32**, 281–289.
47 R. Aoyagi, H. Takeda, S. Okamura and T. Shiosaki, *Mater. Res. Bull.*, 2003, **38**, 25–32.
48 A. Snedden, K. S. Knight and P. Lightfoot, *J. Solid State Chem.*, 2003, **173**, 309–313.
49 V. M. Goldschmidt, *Naturwissenschaften*, 1926, **14**, 477–485.
50 N. A. Benedek, *Inorg. Chem.*, 2014, **53**, 3769–3777.
51 V. A. Cascos, J. Roberts-Watts, C. Skingle, I. Levin, W. G. Zhang, P. S. Halasyamani, M. C. Stennett, N. C. Hyatt, E. Bousquet and E. E. McCabe, *Chem. Mater.*, 2020, **32**, 8700–8712.
52 E. E. McCabe, E. Bousquet, C. P. J. Stockdale, C. A. Deacon, T. T. Tran, P. S. Halasyamani, M. C. Stennett and N. C. Hyatt, *Chem. Mater.*, 2015, **27**, 8298–8309.